

# DEMOGRAPHIC-AWARE FINE-GRAINED CLASSIFICATION OF PEDIATRIC WRIST FRACTURES

Ammar Ahmed<sup>1</sup> Ali Shariq Imran<sup>1,\*</sup> Zenun Kastrati<sup>2</sup> Sher Muhammad Daudpota<sup>3</sup>

<sup>1</sup> Department of Computer Science (IDI), Norwegian University of Science & Technology (NTNU), Gjøvik, 2815, Norway

<sup>2</sup> Department of Informatics, Linnaeus University, Växjö, 351 95, Sweden

<sup>3</sup> Department of Computer Science, Sukkur IBA University, Sukkur, 65200, Pakistan

## ABSTRACT

Wrist pathologies are frequently observed, particularly among children who constitute the majority of fracture cases. Computer vision presents a promising avenue, contingent upon the availability of extensive datasets, a notable challenge in medical imaging. Therefore, reliance solely on one modality, such as images, proves inadequate, especially in an era of diverse and plentiful data types. This study addresses the problem using a multifaceted approach: framing it as a fine-grained recognition task, fusing patient metadata with X-rays, and leveraging weights from a separate fine-grained dataset rather than from a coarse-grained dataset like ImageNet. Unlike prior work, this is the first application of metadata integration for wrist pathology recognition. Our results show that combining fine-grained transformer approach, fine-grained pre-training, and metadata integration improves diagnostic accuracy by 2% on small custom curated dataset and over 10% on a larger fracture dataset.

**Index Terms**— Pediatric fracture classification, fracture detection, medical X-ray imaging, fine-grained classification, Patient metadata

## 1. INTRODUCTION

Hand injuries are among the most frequent presentations in emergency departments, with wrist fractures accounting for up to 75% of cases [1]. Given the wrist’s complex anatomy and critical role in hand function, accurate diagnosis is essential to prevent long-term impairment. Recent advances in computer vision have shown promise in detecting trauma-related abnormalities on X-rays; however, such methods typically require large, well-annotated datasets, which remain scarce in medical imaging. To overcome this limitation, multimodal learning approaches that combine patient metadata with imaging have been explored in domains such as dermatology and oncology, showing consistent improvements in diagnostic accuracy [2–6].

A consistent trend in these studies is the predictive value of demographic metadata, particularly age and sex. Thomas

et al. [6] demonstrated accuracy gains by fusing age, sex, and anatomical site with dermoscopy images, while Li et al. [5] reported 89.1% accuracy on ISIC 2018 using PNASNet with metadata fusion. Pacheco et al. [7, 8] showed balanced accuracy improvements and introduced specialized fusion modules, and Ningrum et al. [2] achieved 92.3% melanoma classification by coupling ANN-based metadata encoders with CNNs. More recently, Cai et al. [4] applied ViTs with metadata encoders, reaching 93.8% accuracy. Collectively, these works establish metadata as a critical complement to imaging in medical AI.

Despite this progress, metadata integration has not been investigated for wrist pathology classification. This omission is critical because wrist anatomy and pathology presentation are strongly age- and sex-dependent. Carpal ossification occurs in well-defined stages, the distal radial and ulnar physes close at different ages for boys and girls [9, 10], and common pediatric fracture types (e.g., buckle, greenstick) differ from adult patterns [11, 12]. Without age/sex context, a model might misclassify normal developmental features (like unfused growth plates) as abnormalities.

To address this gap, we extend metadata integration to musculoskeletal imaging. We first frame wrist abnormality recognition as a fine-grained visual recognition (FGVR) task, unlike prior multimodal efforts that primarily used conventional CNNs. On top of this, we fuse demographic metadata with radiographs to capture subtle, age- and sex-specific morphological cues that image-only models often overlook. Building on our prior work image-only fine-grained recognition work [13, 14], we propose a joint framework for pediatric wrist pathology analysis and hypothesize that it will outperform image-only and CNN-based baselines.

## 2. METHODS

### 2.1. Dataset Curation & Patient Metadata

We curated two datasets from GRAZPEDWRI-DX [15]. (1) A “limited” set of three wrist pathologies (fracture, bone anomaly, soft tissue), excluding the “metal” class, follow-

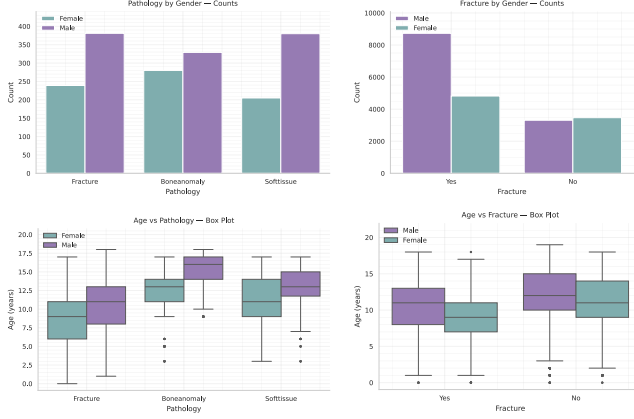


**Fig. 1:** Bar and box plots for gender and age, respectively, for both curated datasets.

ing our prior work [13, 14]. (2) A binary “Fracture vs. No Fracture” dataset using all images, with the non-fracture class augmented for balance. Final splits are shown in Table 1. The cohort included 6,091 patients (2,688 female, 3,402 male, ages 0.2–19 years, mean 10.9). Fig. 1 shows distributions: fractures are more common in males, while anomalies concentrate in older groups.

## 2.2. Architectural Details

This work utilizes a hybrid architecture that integrates both visual data and meta-information, drawing inspiration from the architecture called “MetaFormer” [16]. As depicted in Fig. 2, the architecture is organized into five stages. The first stage (S0) starts with a basic 3-layer convolutional stem, which processes raw input images. Subsequent stages progressively downsample the feature maps and increase channel dimensionality. Stages S1 and S2 consist of MBConv blocks enhanced with squeeze-and-excitation mechanism. The final two stages, S3 and S4, transition to transformer-based blocks that employ relative positional encoding. This design allows the model to capture global dependencies, which are crucial for subtle pathological differences that span larger contexts (e.g., comparing radius vs. ulna contours or detecting diffuse soft tissue swelling).

Downsampling is applied at the beginning of each stage. In S3 and S4, overlapping patch embedding is implemented using convolutions with a stride of 2 and zero-padding, effectively reducing resolution while maintaining contextual overlap [17]. Table 2 outlines the configuration details of the three variants of the architecture used in our experiments.

To overcome the lack of spatial awareness in standard self-attention, the model incorporates a relative position bias. Specifically, a bias matrix  $B \in \mathbb{R}^{((M^2+N) \times (M^2+N))}$  is added during attention computation:

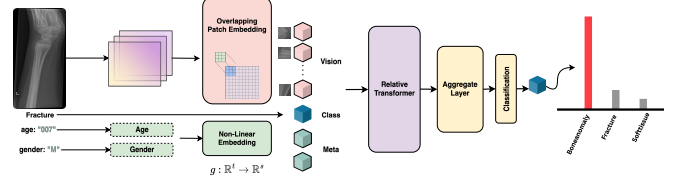


**Fig. 2:** The architecture pipeline integrates visual, class, and meta tokens within a transformer framework.

$$\text{Attention}(Q, K, V) = \text{Softmax} \left( \frac{QK^T}{\sqrt{d}} + B \right) V \quad (1)$$

Here,  $Q$ ,  $K$ , and  $V$  are the query, key, and value matrices of size  $\mathbb{R}^{((M^2+N) \times d)}$ , where  $M^2$  corresponds to the number of image patches and  $N$  is the count of extra tokens (e.g., class and meta tokens). The bias matrix  $B$  is parameterized as described in [18], supporting relative positions from  $-M - 1$  to  $M + 1$ . A shared bias is applied for non-visual tokens since their spatial position is undefined.

The Relative Transformer Block comprises multi-head self-attention (MSA), layer normalization (LN), and a multi-layer perceptron (MLP), applied to the input token sequence  $z_0$ :

$$\begin{aligned} z_0 &= [x_{\text{class}}; x_{\text{meta}}^1, \dots, x_{\text{meta}}^{n-1}; x_{\text{vision}}^1, \dots, x_{\text{vision}}^m] \\ z'_i &= \text{MSA}(\text{LN}(z_{i-1})) + z_i \\ z_i &= \text{MLP}(\text{LN}(z'_i)) + z'_i \end{aligned} \quad (2)$$

In this formulation,  $z_i \in \mathbb{R}^{(M^2+N) \times d}$  captures the updated token sequence at each transformer layer.

Stages S3 and S4 each generate a class token,  $z_{\text{class}}^1$  and  $z_{\text{class}}^2$ , which encode combined visual and meta representations. Since these tokens may differ in dimension,  $z_{\text{class}}^1$  is first projected to match the shape of  $z_{\text{class}}^2$  using an MLP. The two are then concatenated and passed through a 1D convolution followed by normalization:

$$\begin{aligned} \hat{z}_{\text{class}}^1 &= \text{MLP}(\text{LN}(z_{\text{class}}^1)) \\ z_{\text{class}} &= \text{Conv1d}(\text{Concat}(\hat{z}_{\text{class}}^1, z_{\text{class}}^2)) \\ y &= \text{LN}(z_{\text{class}}) \end{aligned} \quad (3)$$

The final output  $y$  aggregates information across multiple scales and token types. When using external attributes as metadata, these are encoded as vectors and embedded using a fully connected non-linear function  $f: \mathbb{R}^n \rightarrow \mathbb{R}^d$ . In our setup, the demographic attributes consist of age and gender. The age attribute was normalized using min–max scaling, while the gender attribute was one-hot encoded. This results in a 2D input vector, which is then projected into the same embedding space as the vision tokens, ensuring consistency between visual and meta representations.

**Table 1:** Instances in training, validation, and test sets.

Three Wrist Pathologies (Limited set)				Fracture vs. No Fracture (Entire set)			
Class	Training	Validation	Test	Class	Training	Validation	Test
Boneanomaly	392	98	119	Fracture	11854	1357	338
Fracture	400	100	120	No Fracture	10164	1357	338
Soft-tissue	376	94	115				
Total	1168	292	354	Total	22018	2714	676

**Table 2:** Configuration of the architecture series. B represents the number of blocks, and H denotes the hidden dimensions for each stage.

Stage	FG-0	FG-1	FG-2
S0	B=3 H=64	B=3 H=64	B=3 H=128
S1	B=2 H=96	B=2 H=96	B=2 H=128
S2	B=3 H=192	B=6 H=192	B=6 H=256
S3	B=5 H=384	B=14 H=384	B=14 H=512
S4	B=2 H=768	B=3 H=768	B=3 H=1024

To maintain the model’s ability to learn important visual features, especially when metadata is less informative or potentially overfitting, a regularization strategy is applied during training that progressively masks parts of the meta-information. This balances the reliance on both vision and auxiliary data.

### 2.3. Experimental Settings

A range of well-established models has been incorporated in our study alongside our fine-grained metadata-aware approach for comparison. All these baseline models were pre-trained on ImageNet [19]. These include ViT [20], VGG16 [21], GoogleNet [22], EfficientNetV2 [23], AlexNet [24], DenseNet201 [25], InceptionV3 [26], and ResNet50 [27]. All models underwent training for 100 epochs using an image resolution of 224x224 and a batch size of 32. Adam optimizer was utilized with a learning rate  $\eta = 5 \times 10^{-3}$ . For MetaFormer, however, the base learning rate was  $\eta = 1 \times 10^{-4}$ , warmup learning rate  $\alpha = 5 \times 10^{-7}$ , minimum learning rate was  $\eta_m = 1 \times 10^{-5}$ , and weight decay was  $\wp = 5 \times 10^{-2}$ .

## 3. RESULTS & DISCUSSION

### 3.1. Baseline Comparison

Table 3 shows that MetaFormer (79.4%) outperforms widely used CNNs such as ResNet50 (77.7%) and DenseNet201 (76.8%). This gives credence to the fact that transformer-based architectures with fine-grained design are better suited to capture subtle morphological cues in pediatric wrist radiographs, where differences between normal anatomy and

**Table 3:** Performance evaluation of different baseline neural networks and the MetaFormer on only image data.

Model	Test Accuracy (Vision Only)
ViT	62.71%
VGG16	63.28%
GoogleNet	70.34%
EfficientNetV2	72.32%
AlexNet	74.29%
DenseNet201	76.84%
InceptionV3	77.44%
ResNet50	77.68%
MetaFormer FGVR (Base)	<b>79.40%</b>

pathology can be minimal.

### 3.2. Metadata Integration & Pretraining

Integrating demographic metadata (age, sex) consistently improved performance (Table 4). Both early and late fusion surpassed vision-only models, with late fusion achieving the highest gains in two out of three configurations. This finding aligns with the intuition that age and sex provide essential developmental context, particularly relevant in pediatrics, where normal ossification patterns vary across individuals. Late fusion may be more robust to noise in individual modalities, as combining information at a later stage allows the final decision to benefit from multiple sources, potentially mitigating the impact of noise or errors in any single modality.

Attribute-level analysis (Table 6) further indicates that both age and sex independently contribute to performance, but their combination yields the largest benefit, supporting the clinical relevance of demographic context.

We then selected the “FG-2” configuration and used the weights obtained from training it on the iNaturalist dataset [28] to create our “FG-2-inat” configuration. This surpassed all other configurations, whether using image data alone or in conjunction with metadata. This configuration reached 81.4%, a 1.5% improvement over image-only training. It seems that the fine-grained pretraining improved generalization beyond ImageNet pretraining, reflecting the value of transferring from domains where subtle inter-class variations dominate. Table 5 shows per class sensitivity, specificity, and precision scores for configuration “FG-2-

**Table 4:** Accuracy of different MetaFormer configurations on only image data, integrating metadata through early fusion, and integrating metadata through late fusion.

Model Configuration	Vision Only	Early Fusion	Late Fusion
FG-0	79.4%	79.1%	80.5%
FG-1	78.5%	80.5%	79.1%
FG-2	77.4%	78.5%	79.4%
<b>FG-2-inat (Ours)</b>	<b>79.9%</b>	<b>81.1%</b>	<b>81.4%</b>

**Table 5:** Evaluation of our configuration of MetaFormer (FG-2-inat) using sensitivity, specificity, and precision.

Configuration	Cls	Sensitivity	Specificity	Precision
Vision Only	0	62.2%	98.7%	96.1%
	1	100%	82.9%	75%
	2	77.4%	88.3%	76.1%
Vision+Meta	0	66.4%	98.7%	96.3%
	1	100%	82.9%	75%
	2	77.4%	90.4%	79.5%

inat”.

On the larger “Fracture vs. No Fracture” dataset (Table 7), metadata integration produced a 10% absolute gain, underscoring the robustness of multimodal learning even when the task is coarser. These results suggest that metadata not only aids fine-grained wrist pathology recognition but also enhances scalability to larger clinical datasets.

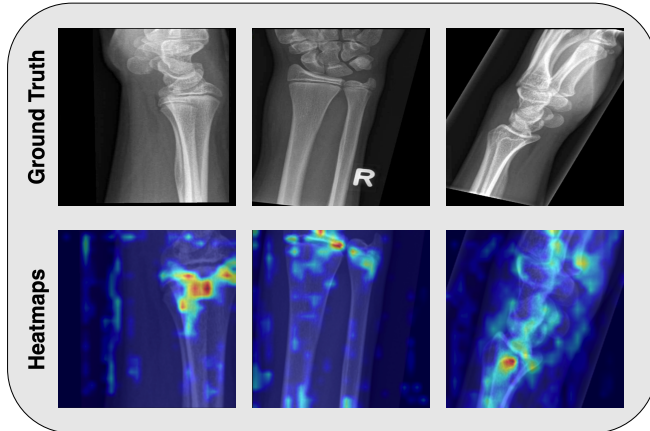


**Fig. 3:** Heatmaps generated from the final convolutional layer in stage 2 (S2) of our configuration “FG-2-inat” on a limited dataset.

### 3.3. Interpretability

GradCAM heatmaps (Fig. 3) demonstrate that MetaFormer attends to clinically relevant wrist regions, particularly around fracture lines and anomalous bone structures. While most heatmaps align well with pathology, some exhibit diffuse at-

**Table 6:** Table showing accuracies obtained by our configuration of MetaFormer on individual metadata attributes and when both attributes are considered.

Attribute	Early Fusion	Late Fusion
Vision + Age	80.5%	79.4%
Vision + Gender	79.9%	80.8%
Vision + Age + Gender	<b>81.1%</b>	<b>81.4%</b>

**Table 7:** Performance evaluation on significantly larger (fracture vs. no fracture) dataset.

FG-2-inat (Ours)	Test Accuracy
Vision Only	50.1%
Vision + Meta	<b>60.4%</b>

tention, suggesting occasional reliance on spurious features. This indicates that while metadata integration improves classification, further refinement is needed for precise localization. Nevertheless, the alignment of salient regions with clinical expectations strengthens confidence in the model’s decision process.

## 4. CONCLUSION

In this study, we demonstrated that integrating patient demographic metadata with image data enhances fine-grained recognition of pediatric wrist pathologies. Overall, our experiments demonstrate three key findings: (1) Fine-grained transformer architectures outperform conventional CNNs for pediatric wrist pathology. (2) Demographic metadata (age, sex) significantly improves recognition, with late fusion being most effective. (3) Fine-grained pretraining enhances generalization, and metadata boosts performance across both limited and large-scale datasets. These results emphasize that integrating developmental context into vision models is not only beneficial but essential for robust pediatric musculoskeletal diagnosis.

## 5. ACKNOWLEDGEMENT

This work was supported by the Curricula Development and Capacity Building in Applied Computer Science for Pakistani Higher Education Institutions (CONNECT) Project

NORPART-2021/10502, funded by the Norwegian Directorate for Higher Education and Skills (DIKU).

## 6. REFERENCES

- [1] Bryan C. MD Hoynak, "Wrist Fracture Management in the ED," Practice Essentials, Pathophysiology, Prognosis, 2022.
- [2] Dina Nur Anggraini Ningrum, Sheng-Po Yuan, Woon-Man Kung, Chieh-Chen Wu, I-Shiang Tzeng, Chu-Ya Huang, Jack Yu-Chuan Li, and Yao-Chin Wang, "Deep Learning Classifier with Patient's Metadata of Dermoscopic Images in Malignant Melanoma Detection," *Journal of Multidisciplinary Healthcare*, vol. 14, pp. 877–885, 2021.
- [3] Fabrizio Nunnari, Chirag Bhuvaneshwara, Abraham Obinwanne Ezema, and Daniel Sonntag, "A Study on the Fusion of Pixels and Patient Metadata in CNN-Based Classification of Skin Lesion Images," in *Machine Learning and Knowledge Extraction*, Andreas Holzinger, Peter Kieseberg, A Min Tjoa, and Edgar Weippl, Eds., pp. 191–208. Springer International Publishing, 2020.
- [4] Gan Cai, Yu Zhu, Yue Wu, Xiaoben Jiang, Jiongyao Ye, and Dawei Yang, "A Multimodal Transformer to Fuse Images and Metadata for Skin Disease Classification," *The Visual Computer*, vol. 39, no. 7, pp. 2781–2793, 2023.
- [5] Weipeng Li, Jiaxin Zhuang, Ruixuan Wang, Jianguo Zhang, and Wei-Shi Zheng, "Fusing metadata and dermoscopy images for skin disease diagnosis,".
- [6] Spencer A. Thomas, "Combining Image Features and Patient Metadata to Enhance Transfer Learning," in *2021 43rd Annual International Conference of the IEEE Engineering in Medicine and Biology Society (EMBC)*, 2021, pp. 2660–2663.
- [7] Andre G. C. Pacheco and Renato A. Krohling, "The Impact of Patient Clinical Information on Automated Skin Cancer Detection," *Computers in Biology and Medicine*, vol. 116, pp. 103545, 2020.
- [8] Andre G. C. Pacheco, and Renato A. Krohling, "An Attention-Based Mechanism to Combine Images and Metadata in Deep Learning Models Applied to Skin Cancer Classification," *IEEE Journal of Biomedical and Health Informatics*, vol. 25, no. 9, pp. 3554–3563, 2021.
- [9] Namazi H;Khaje R, "Normal age-related alterations on distal radius radiography," *The archives of bone and joint surgery*, vol. 3, no. 4, 2015.
- [10] Ki Yap, Craig Hacking, and Jeremy Jones, "Ossification centres of the wrist," *Radiopaedia.org*, Nov 2010.
- [11] Contributors to, "common type of fracture in children," Dec 2020.
- [12] Karen Rosendahl, Ramona Myklebust, Kjersti Foros Ulriksen, A. Nøttveit, Pernille Eide, Åsmund Djuve, and Christina Brudvik, "Incidence, pattern and mechanisms of injuries and fractures in children under two years of age," *BMC Musculoskeletal Disorders*, vol. 22, no. 1, Jun 2021.
- [13] Ammar Ahmed, Ali Shariq Imran, Zenun Kastrati, Sher Muhammad Daudpota, Mohib Ullah, and Waheed Noor, "Learning from the few: Fine-grained approach to pediatric wrist pathology recognition on a limited dataset," *Computers in Biology and Medicine*, vol. 181, pp. 109044, Oct 2024.
- [14] Ammar Ahmed, Ali Shariq Imran, Mohib Ullah, Zenun Kastrati, and Sher Muhammad Daudpota, "Navigating limitations with precision: A fine-grained ensemble approach to wrist pathology recognition on a limited x-ray dataset," in *2024 IEEE International Conference on Image Processing (ICIP)*, 2024, pp. 3077–3083.
- [15] Eszter Nagy, Michael Janisch, Franko Hrzić, Erich Sorantin, and Sebastian Tschauner, "A pediatric wrist trauma x-ray dataset (grazpedwri-dx) for machine learning," *Nature News*, 2022.
- [16] Qishuai Diao, Yi Jiang, Bin Wen, Jia Sun, and Zehuan Yuan, "MetaFormer: A Unified Meta Framework for Fine-Grained Recognition," *arXiv.org*, 2022.
- [17] Wenhai Wang, Enze Xie, Xiang Li, Deng-Ping Fan, Kaitao Song, Ding Liang, Tong Lu, Ping Luo, and Ling Shao, "Pvtv2: Improved Baselines with Pyramid Vision Transformer," *arXiv preprint*, 2021.
- [18] Ze Liu, Yutong Lin, Yue Cao, Han Hu, Yixuan Wei, Zheng Zhang, Stephen Lin, and Baining Guo, "Swin Transformer: Hierarchical Vision Transformer using Shifted Windows," *arXiv preprint*, 3 2021, arXiv:2103.14030.
- [19] Jia Deng, Wei Dong, Richard Socher, Li-Jia Li, Kai Li, and Li Fei-Fei, "Imagenet: A large-scale hierarchical image database," in *Proceedings of the IEEE Conference on Computer Vision and Pattern Recognition (CVPR)*. IEEE, 2009, pp. 248–255.
- [20] Alexey Dosovitskiy, Lucas Beyer, Alexander Kolesnikov, Dirk Weissenborn, Xiaohua Zhai, Thomas Unterthiner, Mostafa Dehghani, Matthias Minderer, Georg Heigold, Sylvain Gelly, Jakob Uszkoreit, and Neil Houlsby, "An Image is Worth 16x16 Words: Transformers for Image Recognition at Scale," 2020.
- [21] Karen Simonyan and Andrew Zisserman, "Very Deep Convolutional Networks for Large-Scale Image Recognition," 2015.
- [22] Christian Szegedy, Wei Liu, Yangqing Jia, Pierre Sermanet, Scott Reed, Dragomir Anguelov, Dumitru Erhan, Vincent Vanhoucke, and Andrew Rabinovich, "Going deeper with convolutions," in *2015 IEEE Conference on Computer Vision and Pattern Recognition (CVPR)*. IEEE, 2015, pp. 1–9.
- [23] Mingxing Tan and Quoc V. Le, "EfficientNetV2: Smaller Models and Faster Training," 2021.
- [24] Alex Krizhevsky, Ilya Sutskever, and Geoffrey E. Hinton, "ImageNet Classification with Deep Convolutional Neural Networks," in *Advances in Neural Information Processing Systems*. 2012.
- [25] Gao Huang, Zhuang Liu, Laurens van der Maaten, and Kilian Q. Weinberger, "Densely Connected Convolutional Networks," 2018.
- [26] Christian Szegedy, Wei Liu, Yangqing Jia, Pierre Sermanet, Scott Reed, Dragomir Anguelov, Dumitru Erhan, Vincent Vanhoucke, and Andrew Rabinovich, "Going Deeper with Convolutions," 2014.
- [27] Kaiming He, Xiangyu Zhang, Shaoqing Ren, and Jian Sun, "Deep Residual Learning for Image Recognition," 2015.
- [28] Grant Van Horn, Oisin Mac Aodha, Yang Song, Yin Cui, Chen Sun, Alex Shepard, Hartwig Adam, Pietro Perona, and Serge Belongie, "The iNaturalist Species Classification and Detection Dataset," *arXiv.org*, April 2018.